RSC Advances

PAPER

View Article Online
View Journal | View Issue

Cite this: *RSC Adv.*, 2026, **16**, 12282

Build-up shielding-factors, and physical & mechanical properties of borosilicate glasses with varied CeO_2 contents

H. A. Abo-Mosallam,[a] Mortaga M. Abou-Krisha,[b] Ahmed A. Galhoum [c] and Ahmed M. A. El-Seidy *[d]

Heavy-metal borosilicate glasses of composition $10BaO–10CdO–12PbO–3Al_2O_3–5SiO_2–(Z)CeO_2–(60 – Z)B_2O_3$ (where Z = 0.5–4.0 mol%) were synthesized *via* a melt-quenching technique to systematically evaluate the influence of CeO_2 incorporation on their γ-ray shielding and mechanical characteristics. XRD and XPS confirmed amorphous glass formation with mixed Ce^{3+}/Ce^{4+} oxidation states (42%/58%), while SEM-EDX evidenced compositional homogeneity and densification with increasing Ce content. Density rose by 8.55%, molar volume decreased by 4.21%, and oxygen packing density increased by 3.48%, signifying structural compaction. Mechanical assessments, based on the Makishima–McKenzie approach, showed that Young's modulus and bulk modulus increased from 74.53 to 77.43 GPa and 51.99 to 56.26 GPa, respectively, up to 2 mol% CeO_2, reflecting enhanced rigidity. Gamma-ray attenuation parameters determined using the Py-MLBUF platform revealed a substantial improvement in linear attenuation coefficient (LAC) by 21.75%, and a reduction in half-value layer (HVL) by 13.64% at 0.015 MeV, confirming superior shielding efficiency. The double-layer exposure buildup factors (DLEBF) reached a maximum of 6.79 at 0.05 MeV for $GC_2–GC_0$, demonstrating effective secondary photon suppression. These results highlight that moderate CeO_2 substitution enhances glass compactness, mechanical resilience, and γ-ray attenuation, establishing Ce-doped borosilicate glasses as robust candidates for advanced radiation shielding applications.

Received 4th February 2026
Accepted 17th February 2026

DOI: 10.1039/d6ra00997b

rsc.li/rsc-advances

1 Introduction

In recent times, rapid and successive development in many aspects of industrial, agricultural and medical life has become an inevitable necessity. In addition, there is an urgent need for energy, which is the backbone of technological development, and providing new sources for it has become extremely important. Today, the use of various types of radioactive materials in many aspects of life, including medicine, military science, space science, and power generation, in addition to many different technological applications, has become inevitable. Therefore, the preparation and development of new types of materials with unique properties for radiation protection has now become an important and vital branch of materials science to avoid the health risks associated with ionizing radiation.[1–3] The efficiency and effectiveness of radiation protection materials can be estimated according to their ability to scatter or absorb ionizing radiation to reduce its danger.[4,5] In the field of radiation shielding materials, many different materials have been used, the most common being concrete and lead. However, in reality, these materials have not met the necessary requirements, resulting in numerous health and environmental effects, in addition to their limited protective efficiency and their degradation over time.[1,6,7] It also requires a significant curing time and specific conditions for optimal performance.[1,6,8]

In the field of materials science for protection from harmful radiation, glass has been greatly appreciated for its promising physical, chemical and optical properties, in addition to its unlimited compositions that meet the changing conditions and requirements of protection.[9–11] Glass systems based on silicates (SiO_2), phosphates (P_2O_5), tellurium oxide (TeO_2), borate (B_2O_3), and a mixture of two or more of these types are the basic nucleus for forming a glass network that is resistant to harmful rays. Of these several glass systems, borate-based glass is the most important and widely used because of its high neutron thermal cross-section and excellent shielding capabilities for both neutron shielding and gamma ray attenuation. The borate glass network can encapsulate various radioactive elements and stabilize them in a stable, non-reactive form.[12–14] Moreover glass

[a]*Glass Research Department, National Research Centre, El-Buhouth St, Dokki, Cairo 12622, Egypt*
[b]*Chemistry Department, College of Science, Imam Mohammad Ibn Saud Islamic University (IMSIU), Riyadh 11623, Saudi Arabia*
[c]*Nuclear Materials Authority, P. O. Box 530, El-Maadi, Cairo, Egypt*
[d]*Inorganic Chemistry Department, Advanced Materials Technology & Mineral Resources Research Institute, National Research Center, 33 El-Bohouth St., Dokki, Cairo, 12622, Egypt. E-mail: am.elseidy@nrc.sci.eg; ahmedmaee2@gmail.com*

optical qualities and radiation shielding capabilities are improved by the adding of subordinate components like heavy metal oxides like ZnO, CdO, BaO and PbO. Recent studies have shown that adding CdO, BaO and lead in varying quantities to borate-based glass modifies the atoms in the internal structure of the glass network and improving its optical properties.[15–17] Furthermore, these elements have strong absorption of ionizing radiation due to their high density. Lanthanide-containing glasses are highly researched and praised for having a low vibration frequency.[18] Cerium (Ce) ion is part of the lanthanide rare earth (RE) ion group and displays promising properties linked to its surface electronic configuration.[19,20] Cerium oxide (CeO_2) is frequently utilized in glass structures because of its beneficial optical, physical, and radiation-shielding qualities.[21,22] To improve shielding glass's ability to absorb radiation, especially gamma and X-ray radiation, cerium oxide (CeO_2) is utilized. It is added to glass compositions to enhance their half-value layer, radiation protection efficiency, and mass attenuation coefficient, making them more potent shields. Additionally, CeO_2 can enhance the glass's optical qualities. The ratios of cerium ions in the host glass composition affect the concentration of the two oxidation states (Ce^{4+}/Ce^{3+}) in which cerium can be integrated into the glassy matrix.[19,23] Although several studies have reported the structural and compositional properties of modified glass systems, a systematic investigation combining structural (XRD), surface chemical (XPS), and microstructural/compositional (SEM-EDS) analyses for the present glass composition and modification range remains limited. The novelty and involvement of the present work lie in providing a comprehensive correlation between compositional modifications and the resulting structural, surface, and elemental characteristics of the glass samples (GC_0–GC_4), supported by experimental evidence. In addition, the objectives of the present study have been clearly stated in a point-wise manner at the end of the Introduction section to improve clarity. In the current studies, the assortment of $10BaO–10CdO–12PbO–5SiO_2–3Al_2O_3–60B_2O_3$ base glass for radiation shielding applications is predicated on their remarkable optical and shielding qualities as well as their exceptional resistance to thermal shocks. Therefore, this work is aimed at doping this unique glass system with varying proportions of cerium oxide (0.5, 1.0, 2.0, and 4.0 mol%) instead of B_2O_3 to investigate how it affects the optical and radiation shielding properties of the prepared glasses. Therefore, the objectives of the present work are as follows: (i) to synthesize and modify glass samples with controlled compositions (GC_0–GC_4), (ii) to investigate the structural properties using XRD, (iii) to examine surface chemical states and bonding environments using (XPS), (iv) to analyze the microstructure and semi-quantitative elemental composition using SEM-EDS, and (v) to correlate compositional modifications with the observed structural and compositional changes.

2 Materials and methods

2.1 Glass synthesis

Barium cadmium lead aluminum borosilicate glasses doped with CeO_2 as a rare earth elements with the composition

Table 1 The elemental fractional abundance and density of the prepared samples

	Glass oxide constitutes (mol%)						
Sample ID	BaO	CdO	PbO	SiO_2	Al_2O_3	CeO_2	B_2O_3
GC_0	10	10	12	5	3	0	60
$GC_{0.5}$	10	10	12	5	3	0.5	59.5
GC_1	10	10	12	5	3	1	59
GC_2	10	10	12	5	3	2	58
GC_4	10	10	12	5	3	4	56

$10BaO–10CdO–12PbO–3Al_2O_3–5SiO_2–(Z)CeO_2–(60 - Z)B_2O_3$ glass system (where $Z = 0$, 0.5, 1, 2, and 4 mol%) were effectively synthesized using the melt quenching technique, as shown in Table 1. Various highly pure chemical reagents of barium carbonate ($BaCO_3$) (99.50%, Loba-Chemie), cadmium carbonate ($CdCO_3$), aluminium oxide (Al_2O_3) (99.90%, Alfa Aesar), Boric acid (H_3BO_3) (ACS reagent, ≥98% Sigma-Aldrich), lead sesquioxide (Pb_2O_3), cerium oxide (CeO_2) oxide with purities of 99.98, and quartz (SiO_2) (99.99%, Alfa Aesar) were weighed to prepare the glass batches. The oxides were thoroughly mixed in an agate mortar to form homogeneous mixtures before melting, which took 90 min in platinum crucibles at temperatures of about 1250 °C in an electrical furnace. The molten glass was stirred several times to remove air bubbles and increase the consistency of the melt. The molten glass was then poured into preheated steel molds and placed in an annealing furnace to relieve stress. The annealing process took place at temperatures around 400 °C for two hours in a muffle furnace, followed by cooling to room temperature at a rate of 1 °C per minute.

2.2 Experimental techniques

XPS measurements were performed using a Thermo Scientific K-Alpha spectrometer (Thermo Fisher Scientific, USA) equipped with a monochromatic Al Kα X-ray source ($h\nu = 1486.6$ eV). The analysis was conducted under ultra-high vacuum conditions (10^{-9} mbar) with a spot size of 400 μm. Survey spectra were recorded with a pass energy of 200 eV, while high-resolution spectra were acquired using a pass energy of 50 eV. Binding energies were calibrated using the C 1s peak at 284.8 eV. Peak deconvolution was carried out after background subtraction using a Shirley background, and curve fitting was performed with appropriate Gaussian–Lorentzian functions. X-ray diffraction (XRD) analysis was carried out using a Bruker D8 Discover diffractometer (Bruker AXS GmbH, Germany) equipped with a Cu target providing CuKα radiation ($\lambda = 1.5406$ Å). The instrument was operated at an accelerating voltage of 40 kV and a current of 40 mA. Data were collected over the selected 2θ range using a step size of 0.02°. SEM observations were carried out using a Prisma E-SEM instrument (Thermo Fisher Scientific Inc., Waltham, MA, USA) equipped with an energy-dispersive X-ray spectroscopy (EDX, Ultradry EDX detector) detector. The analyses were performed at an accelerating voltage of 20–30 kV, with a counting time of 60–120 s and an electron beam diameter of approximately 1–2 μm.

2.3 Density calculations

The density was determined using Archimedes' Principle, as expressed in eqn (1).

$$\rho = \frac{W_{\text{air}}}{W_{\text{air}} - W_{\text{xylene}}} \times \rho_{\text{xylene}}. \quad (1)$$

The symbol ρ represents the density of the glass sample, whereas (W_{air}) denotes the weight of the glass sample in air. The variable (W_{xylene}) represents the weight of the glass sample while immersed in xylene, and ρ_{xylene} is the density of see xylene (??).

2.4 Mechanical study

The primary challenge in the Makishima–McKenzie principle is utilizing the following relations to determine the total ionic packing density (V_t) and the total dissociation energy per unit volume (G_t) for the glass system oxides:

$$V_t = \left(\frac{1}{V_m}\right)\sum_i V_i x_i \quad (2)$$

$$G_t = \sum_i G_i x_i \quad (3)$$

The packing density factor (V_i) and the dissociation energy per unit volume of the supplied glass systems oxides (G_i) are represented by these variables.[24–26] The synthesized specimens' elastic modulus was designed to theoretically extend the Makishima–McKenzie model.[24–26]

2.5 % of change

To investigate the change % on changing from A value to B value, the eqn (4) was used

$$\%\ \text{of change} = \frac{(B\ \text{value} - A\ \text{value}) \times 100}{A\ \text{value}} \quad (4)$$

2.6 Gamma shielding

Py-MLBUF[27,28] were used to calculate linear attenuation coefficient (LAC), mass attenuation coefficient (MAC), half-value layer (HVL), tenth value layer (TVL) and effective atomic number for attenuation (Z_{eff}). The atomic interaction cross section for attenuation (σ-atomic) and electron interaction cross section for attenuation (σ-electron) against energy were also investigated. The buildup factors are correction variables that take into consideration the impact of secondary particles in the materials and scattered radiation. The exposure buildup factor (EBF) and energy absorption buildup factor (EABF) were investigated for single layer and the double layer buildup factors (DLEABF and DLEBF) were examined for double layer shield. The combination of double layers was set as AB and BA with all glass samples as 1st and then as 2nd layer.

Py-MLBUF platform was validated in detailed for 32 materials including standard, plastics and polymers, pure-compounds, fatty-acids, building-materials.[27,29] Fundamental parameters including atomic weights and gamma-photons' cross-sections for the first 92 elements of the periodic table were obtained from NIST: XCOM and XAAMDI[30,31] and the standard values of GPF-parameters for 23 elements were obtained from the ANS-standard.[32] The effects of photons scattering while passing through a Gamma-ray Shielding Parameters (GSP) are described by BUF. The online platforms supports up to 15 layers, before applying the overestimation-correction in the Py-MLBUF this led to some errors in the calculation. In current study only single and double layers were investigated for more accurate results.[33]

The total MAC $(\mu\cdot\rho^{-1})_{\text{Total}}$ for the material is the sum of the coefficients of photoelectric absorption $(\mu\cdot\rho^{-1})_{\text{pe}}$, Compton scattering $(\mu\cdot\rho^{-1})_{\text{cs}}$ and pair production $(\mu\cdot\rho^{-1})_{\text{pp}}$ (eqn (5)).[34]

$$(\mu\cdot\rho^{-1})_{\text{Total}} = (\mu\cdot\rho^{-1})_{\text{pe}} + (\mu\cdot\rho^{-1})_{\text{cs}} + (\mu\cdot\rho^{-1})_{\text{pp}} \quad (5)$$

where μ is LAC and ρ is the density of the selected sample. The true mass absorption coefficient is given by eqn (6)

$$(\mu\cdot\rho^{-1})_{\text{en}} = (\mu\cdot\rho^{-1})_{\text{pe}} + (\mu\cdot\rho^{-1})_{\text{cs}} + (\mu\cdot\rho^{-1})_{\text{pp}} \times \left(\frac{E-1.02}{E}\right) \quad (6)$$

where E is the incident photon energy. Using eqn (7) Z_{eq} can be interpolation whose ratio $(\mu\cdot\rho^{-1})_{\text{cs}}/(\mu\cdot\rho^{-1})_{\text{Total}}$ lies in between two successive ratios of elements.

$$Z_{\text{eq}} = \frac{Z_1(\log\ R_2 - \log R) + Z_2(\log R - \log R_1)}{\log R_2 - \log R_1} \quad (7)$$

where Z_1 and Z_2 are the elemental atomic numbers, R_1 and R_2 corresponding to the ratios, respectively, and R is the ratio for the selected material at the specified energy; $R_1 < R < R_2$.

The equivalent atomic numbers are averaged over the 25 incident photon-E and the atomic number so obtained is treated as the effective atomic number Z_{eff} of that sample for given energy range (eqn (8))

$$Z_{\text{eff}} = \sum_{B=0.015}^{15.0} \frac{Z_{\text{eq}}}{25} \quad (8)$$

The buildup factors were calculated according to eqn (9) and eqn (9) using GP within the energy spectrum of 0.015–15 MeV and up to a penetration depth of 40 mean free paths (mfp)

$$B(E,\ x) = 1 + \frac{b-1}{K-1}(K^x - 1) \quad \text{for}\ K \neq 1 \quad (9)$$

$$B(E, x) = 1 + (b-1)x \ \text{for}\ K = 1 \quad (10)$$

The expression $K(E, x)$ denotes the photon dose multiplication factor, which is determined by eqn (11) for $x \leq 40$ mfp.

$$K(E,\ x) = cx^a + d\frac{\tan h\left(\frac{x}{X_k} - 2\right) - \tan h(-2)}{1 - \tan h(-2)} \quad (11)$$

where b is the accumulation factor at 1 mfp, E denotes the energy of the incident photon, and x refers to the distance from

the source to the detector within the medium, measured in units of mfp.

DLEABF and DLEBF are required for calculating the buildup factors for double-layered shields. Eqn (12) and (13) for estimating DLEBF and DLEABF.

$$B(E,\ x) = B_2 + \frac{B_1(X_1) - 1}{B_2(X_1) - 1} C(X_2) x[B_2(X_1 + X_2 - B(X_2))] \quad (12)$$

$$C(X_2) = \begin{cases} e^{-1.08\beta X_2} + 1.13\beta l(-X_2), & \text{HZFLZ}, \\ 0.8l(X_2) + \left(\frac{\gamma}{K}\right)e^{-X_2}, & \text{LZFHZ}. \end{cases} \quad (13)$$

Eqn (12) and (13) $B(X_1, X_2)$ refers to DLEBF (or DLEABF) for the double-layered shields with X_1 and X_2 as mfp of first and second layer's, respectively.

3 Results and discussion

3.1 XPS

The XPS survey spectra of GCe_0 and GCe_4 are shown in Fig. 1a and b. The spectra of all samples showed the presence of Al-2p (72.08–72.25 eV), Si-2p (94.08–102.98), Pb-4f (139.07–143.13 eV), B-1s (192.01–195.00 eV), C-1s (285.23–287.94 eV), Cd-3d (412.41–416.08), O-1s (531.97–534.18 eV), and Ba-3d (780.38–782.19 eV). The extra peak at 901.94 eV in the spectrum of GCe_4 was attributed to Ce-3d. These results support the proposed structures. The fitting of XPS high-resolution spectra (HRSf) was good for most elements except aluminum, which showed a noisy unclear spectrum due to its low content. HRSf of silicon are shown in Fig. 1c and d. The absence of Si^0 is supported by the presence of all peaks above 100 eV.[35] The spectrum of GCe_0 show two doublets at (100.55, 101.13 eV) and (101.84, 102.24 eV) which were attributed to Si^{1+} (O–Si–Si_3, $2p_{3/2}$ and $2p_{1/2}$) and Si^{3+} (O_3–Si–Si, $2p_{3/2}$ and $2p_{1/2}$) with a shift from Si^0 ($2p_{3/2}$) of 1.25 and 2.54 eV, respectively. The ratio of Si^{3+} may be calculated from eqn (14).[36–38] The average oxidation sate may be calculated as "1 × 0.55 + 3 × 0.45 = 1.91" where 0.55 and 0.45 are the ratio of Si^{1+} and Si^{3+}, respectively. The spectrum of GCe_0 show on doublet at 100.99 and 101.39 which were attributed to Si^{2+} (SiO) $2p_{3/2}$ and $2p_{1/2}$, respectively a Shift from Si^0 ($2p_{3/2}$) of 1.69 eV.[36–38]

$$\%\ Si^{3+} = \frac{\sum Si^{3+}\ \text{peaks area}\left(2p_{3/2} + 2p_{1/2}\right) \times 100}{\sum Si\ \text{all peaks}} \quad (14)$$

HRSf of lead showed a doublet @ 142.95–144.29 and 139.64–138.05 eV which may assigned to Pb-$4f_{5/2}$ and Pb-$4f_{7/2}$, respectively for PbO.[39–41] The extra peak appearing around 414 eV in Fig. 2a and b was assigned to Pb-$4d_{5/2}$which further support forming Pb–O bonds.[39,42] HRSf of *B* are shown in Fig. 1g and h. The absence of any peak around 187 eV indicate the absence of elemental Boron.[43] Peaks in 188.95–183.54 eV region were attributed to B–B[44] while those in 191.11–191.47 and 192.27–192.99 eV corresponding to B_2O_3 and substitutional B that occupy O sites, respectively.[40] Peaks in 193.48–194.84 eV region were attributed B=O in B_2O_3.[45] HRSf of C are shown in Fig. 1i and j. The peaks around 284 and 286 eV were assigned to sp^2 hybridized carbon (C=C) and C–OH, respectively.[46,47] The peaks @ 285.21, 288.45, and 292.76 eV were attributed to sp^3 C–C bonding, (C=O)–O, and C–O/π–π * shake-up satellite.[29,48,49] HRSf of Cd (Fig. 2a and b) show doublet in 411.54–411.81 and 404.65–404.98 eV regions which were attributed to Cd-$3d_{3/2}$ and Cd-$3d_{5/2}$ with separation around 6.8 for a single CdO-related phase.[50] HRSf of O are shown in Fig. 1c and d. The peaks in 529.73–531.24 and 532.03–532.28 eV are attributed to MO (Pb–O–Si/PbO_2/CdO) and chemisorbed oxygen/Si–O–Si in bridging oxygen (BO)/Pb–O–Pb.[49,51–53] The peak at 533.14 eV was assigned to Si–OH, which further support the presence of Si^{1+} while that around 537 eV was due to Pb–Cd–O.[53–57] HRSf of Ba (Fig. 2e and f) show doublet in 794.77–795.19 and 779.57–779.99 eV regions which were attributed to Ba-$3d_{3/2}$ and Ba $3d_{5/2}$ peaks of BaO_2, respectively.[58] The absence of any peaks around 775 eV indicate the absence of BaO.[58] HRSf of Ce are shown in Fig. 2g.

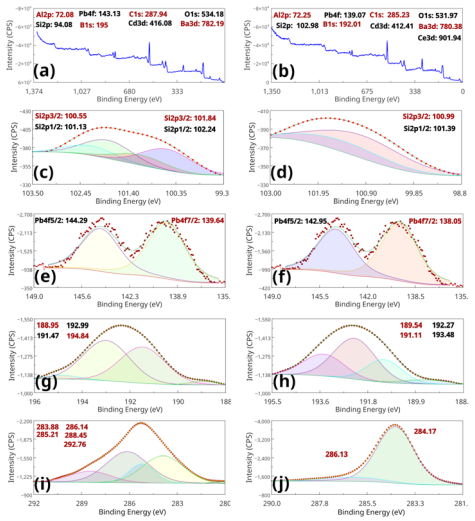

Fig. 1 (a and b) survey spectra, (c and d) HRSf Si, (e and f) HRSf Pb, (g and h) HRSf B and (i and j) HRSf C of GCe_0 and GCe_4.

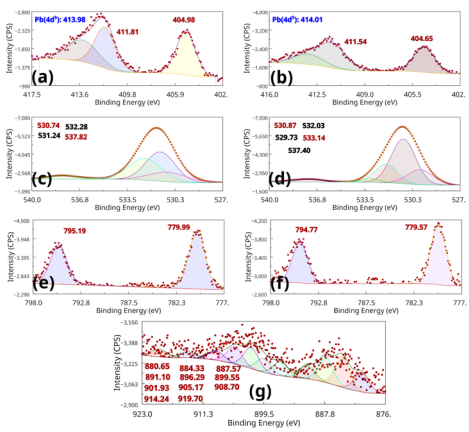

Fig. 2 (a and b) HRSf Cd, (c and d) HRSf, (e and f) HRSf Ba of GCe_0 and GCe_4 and (g) HRSf Ce of GCe_4.

The spectra are complicated because they contain contributions of many components. The interpretation of these spectra indicates the coexistence of both Ce^{3+} ($v_0 + v' + u_0 + u'$) and Ce^{4+} ($v + v' + v''' + u + u' + u'u''' + u'''$) oxidation states.[48,59] The peak u''' is indicated as a fingerprint for +4 state. In these spectra, the u''' was found at 919.70 eV. For +3 state v_0, v', u_0 and u' were found in 880.65, 887.57, 899.55 and 905.17 eV region, respectively. The +4 state v, v'', v''', u, u'', $u'u'''$ and u''' were found at 884.33, 891.10, 896.29, 901.93, 908.70, 914.24 and 919.70 eV region, respectively.[40,48,59,60] The binding energies u/v, u_0/v_0 and $u'/v'/u''/v''$ are the result of O 2p and Ce 4f screening level hydration corresponds to $Ce3d^94f^4O2p^4$, $Ce3d^94f^2O2p^4$, $Ce3d^94f^1O2p^5$ and while u'''/v''' results from $3d^94f^0O2p^6$ final state.[40,48,59,60] The presence of Ce^{3+} can be calculated using the eqn (15). The % Ce^{3+} is 42.00%.

$$Ce^{3+} = \frac{\sum \text{peak area of}(v_0,\ v',\ u_0 \text{ and } u') \times 100}{\text{total peak area}} \quad (15)$$

3.2 XRD

To further confirm the glassy nature of the prepared samples, XRD were performed on three selected samples GCe_0, GCe_2, and GCe_4 as shown in Fig. 3. The XRD analysis of the three specimens showed two distinct broad halos and no sharp diffraction peaks, confirming the amorphous nature of the prepared samples. The presence of two distinct broad halos, with maxima around 28° and 43°, indicates phase separation within the glass [1]. In synthesized glass, separation can be the result from two interpenetrating lead-silicate and borate networks.

3.3 SEM-EDX

The SEM micrographs (Fig. 4a) reveal a clear morphological evolution with Ce addition. The undoped glass (Ce_0), numerous bright inclusions, and surface defects indicate segregation of Pb-, Ba-, and Cd-rich domains within the matrix. These inclusions are often associated with polishing pits and microcracks, reflecting weak mechanical integrity. With progressive Ce addition ($Ce_{0.5}$–Ce_1), the microstructure becomes increasingly uniform; bright heavy-metal-rich features diminish in both number and size, and the background appears smoother and darker (*i.e.*, pull-outs or pits are reduced), indicating reduced modifier segregation and improved glass homogeneity. At higher Ce levels (Ce_2–Ce_4), the surfaces display a nearly featureless, homogeneous matrix with only sparse, submicron inclusions, confirming the depletion of heavy-metal modifiers and enhanced polymerization of the boro-alumino-silicate network. The reduction of pull-outs and cracks further suggests improved stability and mechanical strength with Ce doping. Notably, the bright regions are likely artifacts caused by sample charging under the electron beam.[61]

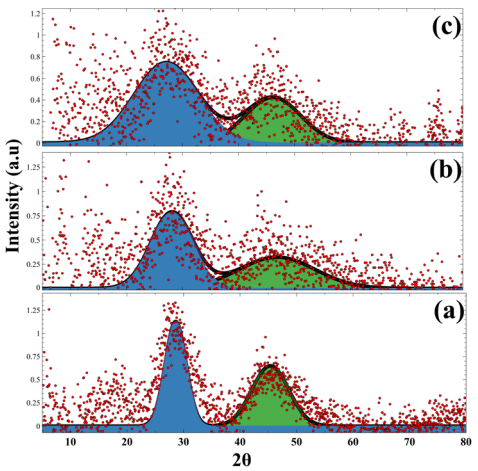

Fig. 3 XRD fitting of (a) GCe_0, (b) GCe_2 and (c) GCe_4.

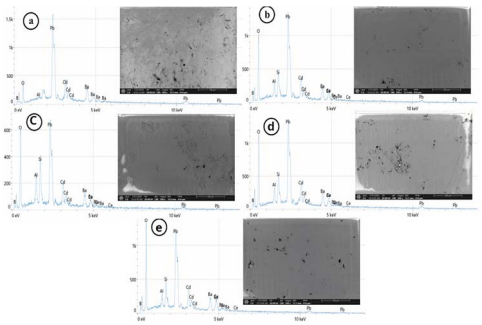

Fig. 4 SEM micrograph and corresponding EDX spectra for samples Ce_0 to Ce_4 (a–e).

The EDX data reveal a complex narrative far beyond a simple doping process for this Ce-doped heavy-metal oxide glass. The presence of B, Si, and Al confirms a boro-alumino-silicate network, providing chemical durability and thermal stability, while the heavy metals (Cd, Ba, Pb) act as modifiers that disrupt the network to impart high density and specific optical properties. The EDX spectra (Fig. 4) confirm the presence of all expected elements in the glass matrix. Cerium is identified by its characteristic $L\alpha$ (4.840 keV), $L\beta_1$ (5.262 keV), and $L\gamma$ (6.052 keV) peaks. Strong $K\alpha$ signals corresponding to B (0.183 keV), O (0.523 keV), Al (1.487 keV), and Si (1.740 keV) further verify the glass-forming network.[61] Pb is distinguished by its $L\alpha_2$ (10.731 keV) and $L\beta_2$ (12.980 keV) lines, while Cd exhibits $L\alpha_1$ (3.133 keV), $L\beta_1$ (3.317 keV), and $L\beta_2$ (3.528 keV) peaks. Ba is detected *via* its $L\alpha_2$ (4.634 keV), $L\alpha_1$ (4.651 keV), $L\beta_1$ (5.042 keV), and $L\beta_2$ (5.384 keV) signals. EDX analysis was conducted on the undoped control sample (Ce_0) and the Ce-doped samples ($Ce_{0.5}$ to Ce_4) to assess material purity and trace changes in elemental composition.[62] This technique confirms the material purity and provides semi-quantitative information on the elemental composition of the samples. EDX analysis was employed to compare and monitor changes in the elemental composition of the glass samples before modification (GC_0; as a control) and after modification for samples $GC_{0.5}$–GC_4. The semi-quantitative results are provided in Table 2. Although the analysis successfully confirms the increasing incorporation of cerium from 0 to 4.9% weight percent (wt%), the most striking observation is the profound compositional shift within the glass matrix itself. The introduction of CeO_2 appears to trigger

Table 2 EDX analysis for the Ce_0 to Ce_4 glass samples

	Ce_0		$Ce_{0.5}$		Ce_1		Ce_2		Ce_4	
Sample element	Atomic %	Weight %	Atomic %	Weight %	Atomic %	Weight %	Atomic %	Weight %	Atomic %	Weight %
B	4.4 ± 0.3	0.7 ± 0.0	8.9 ± 0.3	3.2 ± 0.1	6.8 ± 0.4	2.4 ± 0.1	8.3 ± 0.3	2.8 ± 0.1	9.3 ± 0.3	3.4 ± 0.1
O	51.2 ± 1.2	12.1 ± 0.3	71.1 ± 0.6	37.3 ± 0.3	68.0 ± 0.7	35.2 ± 0.3	69.8 ± 0.5	34.9 ± 0.3	72.2 ± 0.5	39.1 ± 0.3
Al	1.8 ± 0.2	0.7 ± 0.1	3.5 ± 0.1	3.1 ± 0.1	5.9 ± 0.1	5.1 ± 0.1	3.9 ± 0.1	3.3 ± 0.1	2.9 ± 0.2	2.6 ± 0.1
Si	5.1 ± 0.2	2.1 ± 0.1	5.6 ± 0.2	5.2 ± 0.1	9.2 ± 0.1	8.4 ± 0.1	6.8 ± 0.2	6.0 ± 0.2	5.3 ± 0.1	5.1 ± 0.1
Cd	12.4 ± 0.3	20.6 ± 0.5	4.2 ± 0.1	15.7 ± 0.3	3.4 ± 0.2	12.4 ± 0.5	3.3 ± 0.1	11.5 ± 0.4	3.4 ± 0.1	13.1 ± 0.4
Ba	12.7 ± 0.1	25.7 ± 0.3	4.2 ± 0.1	18.7 ± 0.4	3.2 ± 0.1	14.3 ± 0.5	3.8 ± 0.1	16.3 ± 0.4	3.8 ± 0.1	17.5 ± 0.2
Ce	0.0 ± 0.0	0.0 ± 0.0	0.2 ± 0.1	0.9 ± 0.3	0.2 ± 0.1	1.0 ± 0.2	0.6 ± 0.1	2.8 ± 0.2	1.0 ± 0.1	4.9 ± 0.1
Pb	12.5 ± 0.1	38.1 ± 0.4	2.4 ± 0.0	16.0 ± 0.2	3.2 ± 0.1	21.2 ± 0.3	3.5 ± 0.1	22.5 ± 0.3	2.0 ± 0.0	14.3 ± 0.2
Total	100	100	100	100	100	100	100	100	100	100

a substantial restructuring, evidenced by a dramatic decrease in the concentration of the heavy metal constituents and a corresponding increase in the glass formers (B, O, Si, Al). The key trends and observations are as follows:

• Cerium content successfully increases from 0.0 to 1.0 in at% (~0.0 to 4.9 in wt%), confirming effective doping. The progression is not perfectly linear (*e.g.*, $Ce_{0.5}$ and Ce_1 are similar), which is common in synthesis due to factors like volatilization or solubility limits. The significant jump between Ce_1 and Ce_2/Ce_4 is notable.

• The atomic concentrations of the heavy metal modifiers (Cd, Ba, and Pb), plummet from a combined ~37 at% in the Ce_0 blank to roughly ~13% in atomic percent (at%) for all doped samples. Their concentrations plummet at Ce_0 then remain low: Pb: (drops from 12.5 at% to 3.6 at%), Cd (drops from 12.4 at% to 5.0 at%), Ba (drops from 12.7 at% to ~4.6 at%).

• Glass formers and intermediates (O, B, Si, Al): their concentrations in atomic percent (at%) increase significantly as follows: O increases from 51.2% to over 72.2%, B increases from 4.4% to 9.3%. While Si and Al display fluctuating, non-linear concentration trends across the series. Despite this variability, their atomic percentages are consistently higher in the Ce-doped samples relative to the blank (Ce_0) glass.

• The significant increase in oxygen atomic percent (from ~51% to ~72%) cannot be explained by the cerium oxide (CeO_2 or Ce_2O_3) addition alone. This serves as a crucial clue that the doped samples ($Ce_{0.5}$–Ce_4) were synthesized from a base composition that was fundamentally different from the Ce_0 blank from the outset.

These observed restructuring suggests two interpretations: the doped series may have utilized an intentionally altered base composition to aid cerium incorporation, or, if a single batch was targeted, the addition of oxidizing CeO_2 potentially initiated redox reactions that volatilized heavy metals or enhanced crucible corrosion. Consequently, the Ce_4 glass constitutes a distinct material—enriched in oxides and depleted in heavy metals—rather than a simple cerium-admixed variant of Ce_0. This is a pivotal finding; clarifying its origin by consulting batch sheets and employing XPS and XRD to determine cerium valence and crystallinity is essential before linking these structural changes to the material's functional properties.

3.4 Physical properties

Density is one of the most important physical properties of glass.[41,49] Table 3 indicate an improvement in density with CeO_2/B_2O_3 replacement by 2.11%, 3.68%, 6.47% and 8.55% for $\frac{CeO_2}{B_2O_3} = \frac{0.50}{59.50}$ ($GC_{0.5}$), $\frac{1.00}{59.00}$ (GC_1 G), $\frac{2.00}{58.00}$ (GC_2) and $\frac{4.00}{56.00}$ (GC_4), respectively. This results may be due to the density difference between CeO_2 (7.22 g cm^{-3}) and B_2O_3 (2.46 g cm^{-3}).

The samples molar volume (V_m) were calculated using eqn (16):

$$V_m = \frac{\sum x_i M_{wt-i}}{\rho_i} \quad (16)$$

where, x_i = molar fraction and M_{wt-i} = molar mass fraction.

Table 3 and Fig. 5 show a decrease in V_m value by 1.58%, 2.59%, 4.20% and 4.21% as the CeO_2 content increase. These values indicate a compression in the glass which were attributed to the increase in cation coordination number (CeO_2: 8, B_2O_3: 3) and the density difference between CeO_2 (7.22 g cm^{-3}) and B_2O_3 (2.46 g cm^{-3}). The difference between GC_2 and GC_4 is very low which may be due the small difference in density and the with double the CeO_2 content and also the number of oxygen atoms per molecule (CeO_2 (2 atoms) and B_2O_3 (3 atoms)). Oxygen packing density (OPD) was calculated using eqn (17):

$$OPD = \frac{c \times \rho \times 10^3}{M_{wt}} \quad (17)$$

Table 3 Physical properties of prepared glass depending on variation in CeO_2 and B_2O_3 concentration

	GC_0	$GC_{0.5}$	GC_1	GC_2	GC_4
Density × 10^{-1}	38.81	39.63	40.24	41.32	42.13
V_m value	26.49	26.07	25.80	25.37	25.37
OPD	87.22	88.43	89.15	90.25	89.47
V_O value	11.47	11.31	11.22	11.08	11.18
V_m^B	33.11	32.18	31.46	30.21	28.83
$d_{B-B} \times 10^{-8}$	3.80	3.77	3.74	3.69	3.63
$n_b \times 10^{22}$ m^{-3}	8.78	8.98	9.13	9.40	9.64
$N \times 10^{20}$ CeO_2	0	1.16	2.33	4.75	9.50
R_p (angstrom) CeO_2	—	8.28	6.55	5.17	4.10
R_i (angstrom) CeO_2	—	20.53	16.24	12.82	10.17

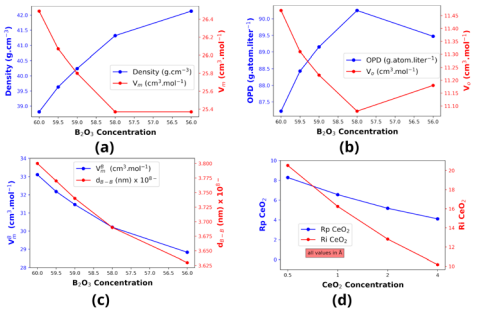

Fig. 5 Effect of CeO_2 replacement of B_2O_3 on (a) density, and V_m, (b) OPD, and V_o, (c) V_m^B, and d_{B-B}, (d) R_p CeO_2 and R_i CeO_2.

where, c = the number of oxygen's in the glasses, ρ = the density and M_{wt} = sum of molar mass fraction.

The OPD is the next most important physical property of glass after density. Table 3 and Fig. 5b show the OPD values, which showed a general increase from by 1.39%, 2.22%, 3.48% and 2.58% with increasing CeO_2 content. The increase in OPD values is strongly related to the increase in density and also the higher C_{no} of CeO_2 (8) compared to that of B_2O_3 (3). Other physical parameters were calculated using:

$$V_o = \frac{V_m}{\sum x_i \times n_i} \tag{18}$$

$$V_m{}^B = \frac{V_{m-i}}{2(1 - X_B)} \tag{19}$$

$$d_{<B-B>} = \left(\frac{V_m{}^B}{2(1 - X_B)}\right)^{\frac{1}{3}} \tag{20}$$

$$N = \frac{X_{Cu} \times \rho \times Na}{M_w} \tag{21}$$

$$R_p = \frac{1}{2}\left(\frac{\pi}{6N}\right)^{\frac{1}{3}} \tag{22}$$

$$R_i = \left(\frac{1}{N}\right)^{\frac{1}{3}} \tag{23}$$

$$n_b = \frac{Na \times \sum x_i \times n_f}{V_m} \tag{24}$$

where V_o: the oxygen molar volume, V_m^B: boron atom molar volume, d_{B-B}: average boron–boron separation, x_B: molar fraction of B_2O_3, Na: Avogadro's number (6.0228 × 1023 g mol^{-1}), N: ionic concentration, R_p: polaron radius, R_i: inter-ionic distance, and n_b: bonds per unit volume.

V_o values (Table 3 and Fig. 5b) show the exact same behavior as V_m, decreasing from 11.47 (GC_0) to 11.08 at GC_2 then increases to 11.18 at GC_2. These values indicate a compression in V_o which as stated before is due to the higher density and cation coordination number of CeO_2. After CeO_2 the most effective factor is the number of oxygen atoms in molecule. The decrease in both V_o and V_m indicate a compression in glass structural network which in turns explain the decrease in $d_{<B-B>}$ and V_m^B values (Table 3 and Fig. 5c). The value of N, R_p and R_i were calculated depending on the variation of CeO_2 concentrations as can be seen in Table 3 and Fig. 5d. The values of N,

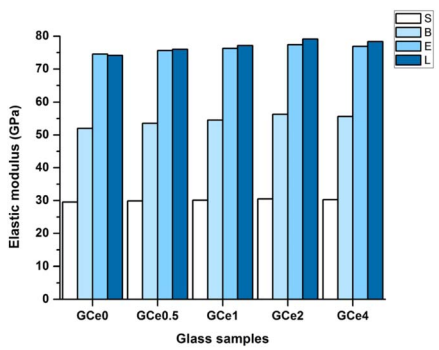

Fig. 6 The elastic modulus of the synthesized glasses Young's modulus, E; bulk modulus, B; shear modulus, S; and longitudinal modulus L.

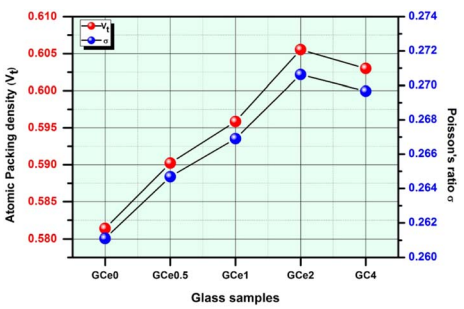

Fig. 7 Atomic packing density (V_t) and Poisson ratio (σ) of the investigated YSBP.

Table 4 The elemental fractional abundance and density of the prepared samples[a]

Glass ID	GC_0	$GC_{0.5}$	GC_1	GC_2	GC_4
Young's modulus EM-M (GPa)	745.27	756.13	762.85	774.25	769.02
Shear modulus SM-M (GPa)	295.48	298.94	301.07	304.67	302.84
Longitudinal modulus LM-M (GPa)	741.55	759.74	771.26	791.10	783.59
Bulk modulus BM-M (GPa)	519.94	535.54	545.46	562.60	556.45
V_t	5.81	5.90	0.5.96	6.06	0.6.03
Poisson ratio (σ)	2.61	2.65	2.67	2.71	2.70

[a] All values × 10^{-1}.

Table 5 MAC, LAC and Z_{eff} for prepared glass calculated using Py-MLBUF

	Total MAC ($cm^2\ g^{-1}$)					LAC (cm^{-1})					Z_{eff}				
Energy MeV	GC_0	$GC_{0.5}$	GC_1	GC_2	GC_4	GC_0	$GC_{0.5}$	GC_1	GC_2	GC_4	GC_0	$GC_{0.5}$	GC_1	GC_2	GC_4
0.0150	41.03	41.308	41.585	42.128	43.185	159.24	163.7	167.34	174.07	181.94	59.4448	59.4482	59.4522	59.4587	59.4715
0.0200	27.381	27.469	27.556	27.727	28.059	106.27	108.86	110.88	114.57	118.21	64.6337	64.593	64.5536	64.4758	64.3283
0.0263	13.379	13.419	13.459	13.538	13.69	51.925	53.181	54.16	55.937	57.675	63.6235	63.5993	63.5759	63.5296	63.4415
0.0300	12.974	12.985	12.996	13.017	13.059	50.352	51.459	52.295	53.787	55.016	57.9692	57.9878	58.0062	58.0418	58.1113
0.0400	8.8346	8.8256	8.817	8.7995	8.7659	34.287	34.976	35.48	36.36	36.931	55.5623	55.5907	55.6196	55.6756	55.7864
0.0500	4.9664	5.0444	5.1219	5.2742	5.5701	19.275	19.991	20.611	21.793	23.467	53.0818	53.201	53.317	53.5352	53.9302
0.0595	3.1645	3.2138	3.2628	3.359	3.546	12.282	12.736	13.129	13.879	14.939	50.2044	50.3775	50.546	50.8648	51.4456
0.0600	3.1023	3.1506	3.1986	3.2929	3.4762	12.04	12.486	12.871	13.606	14.645	50.0786	50.254	50.4246	50.7476	51.3361
0.0800	1.5006	1.5227	1.5447	1.588	1.672	5.8238	6.0346	6.216	6.5615	7.044	43.3936	43.6594	43.9192	44.417	45.34
0.1000	1.8807	1.8876	1.8946	1.9082	1.9346	7.2989	7.4807	7.6238	7.8846	8.1507	52.3212	52.4228	52.5234	52.72	53.0985
0.1500	0.72192	0.72399	0.72605	0.7301	0.73796	2.8018	2.8692	2.9216	3.0168	3.109	38.7078	38.8818	39.055	39.3972	40.0684
0.2000	0.39131	0.39217	0.39302	0.39471	0.39798	1.5187	1.5542	1.5815	1.6309	1.6767	29.4158	29.5912	29.7662	30.1148	30.807
0.3000	0.19401	0.19424	0.19448	0.19493	0.19582	0.75296	0.76979	0.78258	0.80547	0.82499	20.3608	20.5024	20.6444	20.9286	21.5001
0.4000	0.13376	0.13384	0.13392	0.13407	0.13437	0.51911	0.53039	0.53888	0.55398	0.56612	16.7619	16.8811	17.0008	17.2411	17.7263
0.5000	0.10648	0.10651	0.10653	0.10658	0.10668	0.41326	0.42209	0.42869	0.4404	0.44944	15.0602	15.1672	15.2748	15.491	15.9284
0.6000	0.091007	0.091008	0.091011	0.091014	0.09102	0.3532	0.36067	0.36623	0.37607	0.38347	14.1402	14.2403	14.3408	14.543	14.9527
0.6620	0.084257	0.084251	0.084245	0.084233	0.08421	0.327	0.33388	0.339	0.34805	0.35478	13.7592	13.8564	13.954	14.1504	14.5485
0.8000	0.073551	0.073534	0.073519	0.073487	0.073425	0.28545	0.29142	0.29584	0.30365	0.30934	13.2174	13.3102	13.4036	13.5914	13.972
1.0000	0.063485	0.063463	0.063442	0.063399	0.063317	0.24639	0.2515	0.25529	0.26196	0.26675	12.7789	12.8682	12.958	13.1386	13.5054
1.1730	0.057473	0.05745	0.057428	0.057383	0.057297	0.22305	0.22767	0.23109	0.23711	0.24139	12.575	12.6627	12.7509	12.9284	13.2886
1.3330	0.053352	0.05333	0.053309	0.053266	0.053184	0.20706	0.21135	0.21451	0.2201	0.22407	12.4747	12.5618	12.6494	12.8256	13.1834
1.5000	0.050063	0.050043	0.050024	0.049985	0.049909	0.1943	0.19832	0.2013	0.20654	0.21027	12.45	12.537	12.6245	12.8006	13.1581
2.0000	0.043632	0.043621	0.043611	0.043589	0.043549	0.16934	0.17287	0.17549	0.18011	0.18347	12.5922	12.6814	12.771	12.9515	13.3177
2.5060	0.039788	0.039787	0.039787	0.039787	0.039786	0.15442	0.15768	0.1601	0.1644	0.16762	12.8974	12.9906	13.0843	13.2726	13.6548
3.0000	0.037356	0.037365	0.037375	0.037393	0.03743	0.14498	0.14808	0.1504	0.15451	0.15769	13.2394	13.337	13.435	13.6321	14.0316
4.0000	0.034462	0.034489	0.034516	0.034569	0.034671	0.13375	0.13668	0.13889	0.14284	0.14607	14.012	14.119	14.2264	14.4423	14.8791
5.0000	0.032989	0.03303	0.033072	0.033153	0.033311	0.12803	0.1309	0.13308	0.13699	0.14034	14.7974	14.9135	15.0302	15.2642	15.7372
6.0000	0.032231	0.032285	0.032339	0.032444	0.032648	0.12509	0.12795	0.13013	0.13406	0.13755	15.5558	15.6803	15.8054	16.056	16.5617
8.0000	0.031807	0.031881	0.031955	0.0321	0.032382	0.12344	0.12634	0.12859	0.13264	0.13642	16.9514	17.0904	17.2298	17.509	18.0704
10.0000	0.032068	0.032158	0.032248	0.032425	0.032769	0.12445	0.12744	0.12977	0.13398	0.13806	18.1704	18.3208	18.4716	18.7732	19.3783
15.0000	0.033636	0.033757	0.033878	0.034115	0.034577	0.13054	0.13378	0.13633	0.14096	0.14567	20.5458	20.7158	20.8858	21.2251	21.9026

R_p and R_i agree with the proposed composition, starting at 0.00 (and no value for R_p and R_i) with no CeO_2 content then increases as the its molar ratio increases.

3.5 Elastic properties RD

The elastic modulus is a fundamental mechanical parameter that measures the stiffness of radiation shielding materials. It plays a crucial role in achieving long-term stability of mechanical strength under various and harsh environmental conditions. The high modulus of elasticity of various materials provides a great ability to resist stresses, enhancing their resistance to structural deformation during use. The calculated basic elastic moduli of the prepared glass materials and the effect of CeO_2/B_2O_3 replacements on the change in these values are shown in Fig. 6 and Table 4. An established approach for figuring out the mechanical characteristics of glass systems is the Makishima and Mackenzie model.[63,64] The elastic modules parameters for the synthesized non-crystalline materials were as shadows: Young's modulus (E) range from 74.527 GPa to 77.425 GPa; Bulk modulus (B) range from 51.994 GPa to 56.260 GPa; Shear modulus (S) range from 29.548 GPa to 30.467 GPa; and Longitudinal modulus (L) range from 74.155 GPa to 79.110 GPa. The mechanical characteristics indicate an increasing trend with CeO_2 content up to 2 mol%, as illustrated in Fig. 6 and Table 4. The reason for the increase in mechanical resistance of the sample prepared by adding the rapid up to 2 mol percent can be attributed to the increase in the number of bridging oxygen compared to the non-bridging oxygen. There is a direct relationship between the amount of bound oxygen and its effect on increasing the strength of the internal structure of the glass and its reflection on the increase in the calculated mechanical resistance.[65] It was found that adding CeO_2 to alkali borosilicate glasses works primarily to strengthen the glass network and is reflected in increasing the mechanical resistance of the prepared glass.[66] On the other hand, the slightly decrease in elastic modulus with increase in cerium dioxide up to 4 mol% can be attributed to role of cerium in increasing the BO_3/BO_4 ratio and decrease the strength of the glass network.[66] It is clear from Table 4 that the relationship between atomic packing density (V_t) and Poisson ratio (σ) is a direct relationship, and the values of both are increased with the increase cerium oxide up to 2 mol%. Poisson's ratio (σ) is frequently used to explain the compactness of glass and the effect of changes in composition on modifications in the cross link density of glass network.[67] Increasing Poisson's ratio values indicate that the internal structure of the glass has become stronger and more toughness.[67] However, the weakened glass network is responsible for the drop in the (V_t) and σ values at 4 mol% (Fig. 7).

3.6 Shielding properties

Single layer shielding properties of current glass samples were investigated using Py-MLBUF by calculating LAC, MAC, HVL, TVL and Z_{eff} in the energy ranges from 0.015 to 15 MeV (Table 5 and Fig. 8). In all samples, LAC values show maximum value at 0.05 eV followed by a sharp decrease then gradual decrease with increasing γE. This general behavior for most materials.[29,46] These values depend mainly on the dominant interaction mechanism. At low γE (0.015 eV) the photoelectric absorption is the dominant but with increasing energy the Compton scattering became more dominant. LAC is a very important factor in considering the efficiency of current glass shielding. The maximum difference between glass samples were noted at lowest γE. LAC of basic glass was improved by 3.71%, 6.93%, 13.06% and 21.75% with $\frac{CeO_2}{B_2O_3} = \frac{0.50}{59.50}$ ($GC_{0.5}$), $\frac{1.00}{59.00}$ (GC_1), $\frac{2.00}{58.00}$ (GC_2) and $\frac{4.00}{56.00}$ (GC_4), respectively. This order agrees with the increase in densities (Table 3). MAC show similar behavior to LAC (Table 5 and Fig. 8b), showing maximum value at 0.05 eV then the values decrease sharply with increasing γE followed by a gradual decrease. The decrease of MAC values as the γE increases may be due to the decrease in the effectiveness of Compton scattering and photoelectric absorption. MAC of basic glass was improved by 1.57%, 3.13%, 6.20% and 5.57% with $\frac{CeO_2}{B_2O_3} = \frac{0.50}{59.50}$ ($GC_{0.5}$), $\frac{1.00}{59.00}$ (GC_1 G), $\frac{2.00}{58.00}$ (GC_2) and $\frac{4.00}{56.00}$ (GC_4), respectively, indicating the superior effect of higher density and molecular weight (CeO_2: 7.22 g cm^{-3}, 174 g mol^{-1}, and B_2O_3: 2.46 g cm^{-3}, 69.62 g mol^{-1}).[37,41,68] The lower Z_{eff} values indicate a higher shielding power at lower γE. The increase of Z_{eff} values (at γE = 1.00 eV: 0.83% ($GC_{0.5}$), 1.66% (GC_1), and 3.32% (GC_2) and 6.65% (GC_4)) with $\frac{CeO_2}{B_2O_3}$

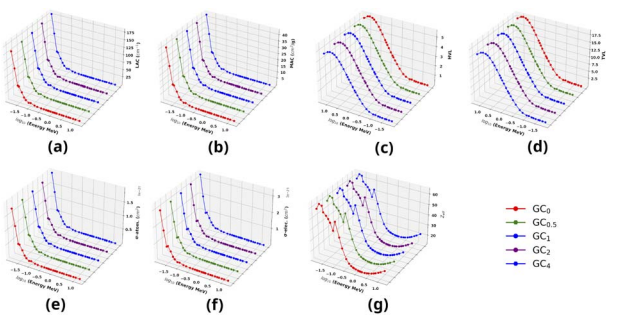

Fig. 8 (a) LAC, (b) total MAC, (c) HVL, (d) TVL, (e) σ-atomic, (f) σ-electron, and (g) Z_{ef} *versus* $\log_{10}$ of photon energy of single layer samples.

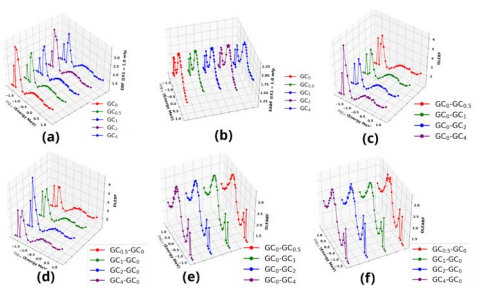

Fig. 9 (a) EBF, (b) EABF and (c & d) DEBF, (e & f) DEABF *versus* $\log_{10}$ of photon energy of single layer samples (selected penetration depth: X_1 = 1 mfp) and of double layers (penetration depth: $X_1 = X_2$ = 1 mfp).

Table 6 HVL, and TVL for prepared glass calculated using Py-MLBUF

	HVL (cm)					TVL (cm)				
Energy MeV	GC_0	$GC_{0.5}$	GC_1	GC_2	GC_4	GC_0	$GC_{0.5}$	GC_1	GC_2	GC_4
0.0150	0.0044	0.0042	0.0041	0.004	0.0038	0.0145	0.0141	0.0138	0.0132	0.0127
0.0200	0.0065	0.0064	0.0063	0.0061	0.0059	0.0217	0.0212	0.0208	0.0201	0.0195
0.0263	0.0133	0.013	0.0128	0.0124	0.012	0.0443	0.0433	0.0425	0.0412	0.0399
0.0300	0.0138	0.0135	0.0133	0.0129	0.0126	0.0457	0.0447	0.044	0.0428	0.0419
0.0400	0.0202	0.0198	0.0195	0.0191	0.0188	0.0672	0.0658	0.0649	0.0633	0.0623
0.0500	0.036	0.0347	0.0336	0.0318	0.0295	0.1195	0.1152	0.1117	0.1057	0.0981
0.0595	0.0564	0.0544	0.0528	0.0499	0.0464	0.1875	0.1808	0.1754	0.1659	0.1541
0.0600	0.0576	0.0555	0.0539	0.0509	0.0473	0.1912	0.1844	0.1789	0.1692	0.1572
0.0800	0.119	0.1149	0.1115	0.1056	0.0984	0.3954	0.3816	0.3704	0.3509	0.3269
0.1000	0.095	0.0927	0.0909	0.0879	0.085	0.3155	0.3078	0.302	0.292	0.2825
0.1500	0.2474	0.2416	0.2372	0.2298	0.2229	0.8218	0.8025	0.7881	0.7633	0.7406
0.2000	0.4564	0.446	0.4383	0.425	0.4134	1.5162	1.4816	1.4559	1.4118	1.3733
0.3000	0.9206	0.9004	0.8857	0.8606	0.8402	3.058	2.9912	2.9423	2.8587	2.791
0.4000	1.3353	1.3069	1.2863	1.2512	1.2244	4.4356	4.3413	4.2729	4.1564	4.0673
0.5000	1.6773	1.6422	1.6169	1.5739	1.5422	5.5718	5.4552	5.3712	5.2284	5.1232
0.6000	1.9625	1.9219	1.8927	1.8431	1.8076	6.5192	6.3843	6.2873	6.1228	6.0046
0.6620	2.1197	2.076	2.0447	1.9915	1.9537	7.0415	6.8963	6.7922	6.6157	6.4902
0.8000	2.4283	2.3786	2.343	2.2827	2.2407	8.0665	7.9014	7.7832	7.5831	7.4435
1.0000	2.8133	2.756	2.7151	2.646	2.5985	9.3455	9.1553	9.0195	8.7897	8.6319
1.1730	3.1075	3.0445	2.9995	2.9234	2.8715	10.323	10.1135	9.964	9.7112	9.5388
1.3330	3.3476	3.2797	3.2312	3.1493	3.0935	11.1204	10.8949	10.7339	10.4617	10.2764
1.5000	3.5675	3.4951	3.4434	3.356	3.2965	11.8509	11.6104	11.4388	11.1486	10.9507
2.0000	4.0933	4.0097	3.9498	3.8485	3.778	13.5978	13.3198	13.121	12.7843	12.5502
2.5060	4.4888	4.396	4.3293	4.2163	4.1352	14.9116	14.6033	14.3818	14.0061	13.737
3.0000	4.7811	4.681	4.6088	4.4861	4.3956	15.8823	15.5499	15.3101	14.9026	14.6018
4.0000	5.1825	5.0713	4.9905	4.8527	4.7454	17.2157	16.8465	16.5781	16.1203	15.7637
5.0000	5.414	5.2953	5.2085	5.06	4.9391	17.9848	17.5907	17.3022	16.8088	16.4075
6.0000	5.5412	5.4175	5.3265	5.1705	5.0393	18.4075	17.9966	17.6943	17.1761	16.7403
8.0000	5.6151	5.4862	5.3905	5.2259	5.0808	18.653	18.2246	17.9068	17.3601	16.8782
10.0000	5.5695	5.4389	5.3415	5.1735	5.0207	18.5014	18.0676	17.7439	17.1859	16.6786
15.0000	5.3098	5.1812	5.0845	4.9172	4.7583	17.6387	17.2116	16.8902	16.3345	15.8068

replacement is due to adding Ce (58) with higher atomic number than B (5).[48,69] σ-atomic, and σ-electron (Table 5 and Fig. 8e, f) show the same behavior, their values decrease as the γE increases, since the probability of the photoelectric effect decreases as photon energy increases.[48,70] HVL and TVL show similar behavior (Table 5 and Fig. 8c, d) showing minimum values at 0.015 eV and increase as the γE increases which indicate the need to increase the thickness with increasing photon energy.[47,71,72] At $\gamma E = 0.0150$ eV:

• HVL: the decrease in valued with increasing $\frac{CeO_2}{B_2O_3}$ content (−4.55% ($GC_{0.5}$), −6.82% (GC_1), −9.09% (GC_2), −13.64% (GC_4)) indicate a higher shielding power (less thickness of the glass).

• TVL: Shaw the same trends (−2.76% ($GC_{0.5}$), −4.83% (GC_1), −8.97% (GC_2), −12.41% (GC_4))

EABF and EBF (single layer) were calculated at 1 mfp as shown in Fig. 9. These are vital in the correction of the attenuation calculation by taking in account the secondary gamma ray emission. EBF_{max} (2.84–3.47) and $EABF_{max}$ (1.63–1.66) are shown in all glass samples in 0.04–0.06 eV region, which result from multiple scattering caused by Compton interaction. To investigate the use of double layer, DLEBF and DLEABF for AB (GC_0 as 1st layer and other samples as 2nd layer), and BA (GC_0 as 2nd layer and other samples as 1st layer) were calculated at $X_1 = 1$ mfp and $X_2 = 1$ mfp penetration depths (Fig. 9). $DLEBF_{max}$ (0.05–0.06) order of current samples was: GC_2–GC_0 (6.792) > GC_0–GC_4 (6.465) > GC_1–GC_0 (4.514) > GC_0–$GC_{0.5}$ (4.505) > GC_4–GC_0 (4.317) > GC_0–GC_2 (4.054) > GC_0–GC_1 (4.017) while that of $DLEABF_{max}$ (0.6–1.0) was GC_0–GC_4 (3.362) > GC_0–GC_2 (3.359) > GC_0–GC_1 (3.357) > GC_4–GC_0 (3.335) > GC_2–GC_0 (3.307) > $GC_{0.5}$–GC_0 (3.227) > GC_1–GC_0 = GC_0–$GC_{0.5}$ (3.166) (Table 6).

4 Conclusion

The present study demonstrates that CeO_2-modified heavy-metal borosilicate glasses exhibit enhanced structural and functional properties, making them promising γ-ray shielding materials. XRD confirmed the fully amorphous nature of all compositions, indicating stable glass networks. SEM-EDS analysis revealed homogeneous microstructures with effective cerium incorporation up to 4.9 wt%. XPS results confirmed mixed Ce^{3+} (42%) and Ce^{40} (58%) states, contributing to improved network cross-linking and structural stability. The addition of CeO_2 significantly influenced the physical and mechanical properties, with glass density increasing by 8.55% from 3.881 g cm^{-3} (GC_0) to 4.213 g cm^{-3} (GC_4), accompanied by a 4.21% reduction in molar volume, reflecting structural compaction. Mechanical modeling revealed enhanced elastic

performance, with Young's modulus, bulk modulus, and shear modulus reaching maximum values of 77.43 GPa, 56.26 GPa, and 30.47 GPa, respectively, at approximately 2 mol% CeO_2. γ-ray shielding performance improved markedly with CeO_2 incorporation, as evidenced by a 21.75% increase in the LAC and a 6.20% rise in the MAC, alongside reductions of 13.64% and 12.41% in the HVL and TVL, respectively, confirming improved photon attenuation efficiency. The Z_{eff} increased by 6.65%, and the maximum double-layer exposure buildup factor ($DLEBF_{max} = 6.79$ at 0.05 MeV) confirmed efficient suppression of secondary radiation. Thus, moderate CeO_2 doping (2 mol%) provides an optimal balance between structural integrity, mechanical strength, and γ-ray attenuation efficiency, positioning these glasses as promising, eco-friendly alternatives to conventional lead-based shielding materials.

Ethical approval

This article doesn't contain any studies involving animals performed by any authors. Also, this article does not contain any studies involving human participants performed by any of the authors.

Consent for publication

All authors have read and agreed to the published version of the manuscript.

Consent to participate

All authors agree to participate in the published version of the manuscript.

Author contributions

H. A. Abo-Mosallam & Mortaga M. Abou-Krisha: synthesis of glass & mechanical study; Ahmed A. Galhoum: SEM-EDX; A. M. A. El-Seidy: shielding/build-up shielding-factors & physical properties; H. A. Abo-Mosallam, Mortaga M. Abou-Krisha, Ahmed A. Galhoum & A. M. A. El-Seidy: writing – review & editing, writing – original draft, validation, methodology, investigation, formal analysis, data curation, conceptualization.

Conflicts of interest

The authors declare that there is no conflict of interest.

Data availability

All data generated or analyzed during this study is included in this published article.

Acknowledgements

This work was supported and funded by the Deanship of Scientific Research at Imam Mohammad Ibn Saud Islamic University (IMSIU) (grant number IMSIU-DDRSP2602).

Notes and references

1 C. G. Hernández-Murillo, L. A. Escalera-Velasco, J. R. M. Contreras, H. R. Vega-Carrillo and H. A. de Leon-Martíne, in *Advanced Radiation Shielding Materials*, Elsevier, 2024, DOI: 10.1016/C2021-0-02858-3.
2 A. Poddar, M. Roy, A. Chamuah and S. Bhattacharya, *Phys. B*, 2026, **723**, 418143.
3 A. Chamuah, K. Bhattacharya, S. Ojha, C. K. Ghosh, J. Ghosh, T. Chakraborty, P. Ranjan and S. Bhattacharya, *Adv. Theory Simul.*, 2025, e01031.
4 M. R. Ahmed, N. A. Alsaif, N. Siddiqui, A. S. Prasad, M. Srinivas, S. K. Ahmmad, K. M. Kaky, A. J. Kadhim and Y. Rammah, *Opt. Mater.*, 2025, **158**, 116461.
5 N. A. Alsaif, N. Alfryyan, H. Al-Ghamdi, Y. Rammah, E. A. Mahdy, H. Abo-Mosallam and F. El-Agawany, *Opt. Mater.*, 2024, **157**, 116081.
6 S. Barbhuiya, B. B. Das, P. Norman and T. Qureshi, *Struct. Concr.*, 2024, **26**, 1809–1855.
7 J. Ghosh, M. S. Ali, R. Sarkar, R. K. Shukla, J. Chowdhury, P. Bhowmick and S. Bhattacharya, *J. Electron. Mater.*, 2025, **54**, 10710–10732.
8 P. Halder, N. D. Sherpa, B. Pahari, N. Roy and S. Bhattacharya, *J. Alloys Compd.*, 2025, **1019**, 179197.
9 G. Annadurai, W. Chaiphaksa, C. Mutuwong, S. Yonphan, Y. Ruangtaweep, W. Cheewasukhanont, N. Intachai, M. Tungjai, S. Kothan, H. Kim and J. Kaewkhao, *Radiat. Phys. Chem.*, 2026, **238**, 113137.
10 D. Keerthana, K. Naseer, S. Arul Raja Sekaran, M. Sayyed, M. S. Alqahtani and K. Marimuthu, *Radiat. Phys. Chem.*, 2026, **238**, 113153.
11 P. Halder, M. S. Ali and S. Bhattacharya, *J. Non-Cryst. Solids*, 2023, **616**, 122459.
12 O. Sallam, M. S. Mansy, Y. Mohamed and N. Elalaily, *Radiat. Phys. Chem.*, 2025, **237**, 113056.
13 E. Ilik, S. H. Guler, O. Guler, H. Durmus, E. Kavaz, S. Birdogan, G. ALMisned, G. Kilic and H. Tekin, *J. Alloys Compd.*, 2025, **1036**, 181904.
14 S. Ojha, A. Chamuah, M. Roy and S. Bhattacharya, *Front. Phys.*, 2023, **11**, year.
15 J. Alyami, Y. Al-Hadeethi, O. A. Fallatah, S. Biradar, M. Sayyed and F. Almutairi, *Ann. Nucl. Energy*, 2025, **212**, 111069.
16 Y. Maghrbi, H. Heryanto, S. Biradar, M. Y. Hanfi and M. Sayyed, *J. Sci.:Adv. Mater. Devices*, 2025, **10**, 100949.
17 K. Bhattacharya and D. Das, *Bull. Mater. Sci.*, 2008, **31**, 467–471.
18 H. H. Negm, A. A. Sdeek and A. A. Ebrahim, *J. Electron. Mater.*, 2024, **53**, 3965–3979.
19 E. Abou Hussein, S. Shaban and S. A. Makhlouf, *Radiat. Phys. Chem.*, 2025, **235**, 112762.
20 D. Das and K. Bhattacharya, *Jpn. J. Appl. Phys.*, 2007, **46**, L1006.
21 A. Acikgoz, G. Demircan, D. Yılmaz, B. Aktas, S. Yalcin and N. Yorulmaz, *Mater. Sci. Eng. B*, 2022, **276**, 115519.

22 K. S. Shaaban, D. A. Aloraini, K. Alsafi, H. M. Almutairi, W. M. Al-Saleh and A. S. Alzahrani, *Mater. Today Commun.*, 2024, **38**, 108309.
23 E. A. Hussein, A. Madbouly, F. E. Eldin and N. ElAlaily, *Mater. Chem. Phys.*, 2021, **261**, 124212.
24 A. Makishima and J. Mackenzie, *J. Non-Cryst. Solids*, 1973, **12**, 35–45.
25 A. Abd El-Moneim, M. A. Azooz, H. A. Hashem, A. M. Fayad and R. L. Elwan, *Sci. Rep.*, 2023, **13**, 1–15.
26 A. Amat, H. M. Kamari, I. Mansor, N. Osman, N. N. S. Nidzam and N. I. M. Kamal, *Appl. Phys. A*, 2021, **127**, year.
27 K. S. Mann and S. S. Mann, *Ann. Nucl. Energy*, 2021, **150**, 107845.
28 O. F. Ozpolat, B. Alım, E. Sakar, M. Büyükyıldız and M. Kurudirek, *Radiat. Environ. Biophys.*, 2020, **59**, 321–329.
29 A. A. Al-Ghamdi, E. E. Bayoumi, S. Al-Farraj, M. Sillanpää and A. M. El-Seidy, *Surf. Interfaces*, 2025, **67**, 106567.
30 S. Seltzer, *XCOM-Photon Cross Sections Database, NIST Standard Reference Database 8*, 1987, DOI: 10.18434/T48G6X.
31 S. Seltzer, *Tables of X-Ray Mass Attenuation Coefficients and Mass Energy-Absorption Coefficients, NIST Standard Reference Database*, 1995, p. 126, DOI: 10.18434/T4D01F.
32 P. Basu, R. Sarangapani and B. Venkatraman, *Appl. Radiat. Isot.*, 2019, **154**, 108864.
33 K. S. Mann, *Nucl. Eng. Technol.*, 2017, **49**, 792–800.
34 K. S. Mann, M. Kurudirek and G. Sidhu, *Appl. Radiat. Isot.*, 2012, **70**, 681–691.
35 A. A. Sokolov, E. O. Filatova, V. V. Afanasev, E. Y. Taracheva, M. M. Brzhezinskaya and A. A. Ovchinnikov, *J. Phys. D: Appl. Phys.*, 2008, **42**, 035308.
36 *Defects in SiO_2 and Related Dielectrics: Science and Technology*, ed. G. Pacchioni, L. Skuja and D. L. Griscom, Springer Netherlands, Dordrecht, 2000, DOI: 10.1007/978-94-010-0944-7.
37 M. S. El-Okaily, A. M. A. El-Seidy, E. H. Ismail, R. M. Allam, A. A. Saeed, A. Bhaumik and A. A. Mostafa, *J. Mater. Res.*, 2024, **39**, 1741–1757.
38 A. M. A. El-Seidy, M. S. El-Okaily, I. M. Nabil and A. A. Mostafa, *Sci. Rep.*, 2025, **15**, year.
39 H.-H. T. Nguyen, Y.-H. Choi, E.-B. Kim, Y.-H. Jeong, J.-W. Lee, K.-H. Park, Y.-J. Woo, S. Ameen and D.-H. Kwak, *Carbon Trends*, 2025, **19**, 100465.
40 O. I. Sallam, Y. S. Rammah, I. M. Nabil and A. M. A. El-Seidy, *Sci. Rep.*, 2024, **14**, 24478.
41 N. A. M. Alsaif, N. Alfryyan, H. Al-Ghamdi, A. M. A. El-Seidy, A. M. Abdelghany, Y. S. Rammah and A. S. Abouhaswa, *J. Inorg. Organomet. Polym. Mater.*, 2024, **34**, 3623–3631.
42 B. Joanne James, R. Cameron and C. Baskcomb, *Res. Lett. Mater. Sci.*, 2008, **2008**, 1–4.
43 T. Susi, T. Pichler and P. Ayala, *Beilstein J. Nanotechnol.*, 2015, **6**, 177–192.
44 S. Zhao, Y. Wu, B. Zhou and X. Liu, *Sci. Rep.*, 2019, **9**, 17337.
45 J. Qu, Q. Li, C. Luo, J. Cheng and X. Hou, *Coatings*, 2018, **8**, 214.
46 A. M. A. El-Seidy, I. E. El-Sayed, M. Linnolahti, E. E. Bayoumi, H. I. Mira and A. A. Galhoum, *RSC Adv.*, 2025, **15**, 28269–28279.
47 A. Elseidy, S. Bashandy, F. Ibrahim, S. Abd El-Rahman, O. Farid, S. Moussa and M. El-Baset, *Egypt. J. Chem.*, 2022, 497.
48 A. M. El-Seidy, M. A. Elbaset, F. A. Ibrahim, S. A. Abdelmottaleb Moussa and S. A. Bashandy, *J. Trace Elem. Med. Biol.*, 2023, **80**, 127312.
49 A. M. A. El-Seidy, O. I. Sallam, I. M. Nabil, Y. S. Rammah, M. S. El-Okaily and H. Alshater, *Sci. Rep.*, 2024, **14**, 25354.
50 S. Rajappan Achary, S. Agouram, J. F. Sánchez-Royo, M. C. Martínez-Tomás and V. Muñoz-Sanjosé, *RSC Adv.*, 2014, **4**, 23137.
51 R. M. Allam, N. M. A. El-Nasr, M. A. Elbaset, D. O. Saleh and A. M. A. El-Seidy, *Sci. Rep.*, 2025, **15**, 15477.
52 R. Svoboda, L. P. Maqueda, V. Podzemná, A. Perejon and O. Svoboda, *J. Non-Cryst. Solids*, 2020, **528**, 119738.
53 J. Du, Z. Zhu, J. Yang, J. Wang and X. Jiang, *Heritage Sci.*, 2021, **9**, 45.
54 I. V. Gordovskaya, T. Hashimoto, J. Walton, M. Curioni, G. E. Thompson and P. Skeldon, *J. Electrochem. Soc.*, 2014, **161**, C601–C606.
55 J. F. Watts and J. Wolstenholme, Comparison of XPS and AES with Other Analytical Techniques, in *An Introduction to Surface Analysis by XPS and AES*, ed. J. F. Watts and J. Wolstenholme, 2019, DOI: 10.1002/9781119417651.ch8.
56 *J. Am. Ceram. Soc.*, 2016, **99**, 363.
57 D. Du, Y. Zeng, C. Wang, M. Li, F. Wang, Z. Xu and H. Wang, *Opt. Mater.*, 2021, **114**, 110957.
58 S. Chakrabarti, S. Ginnaram, S. Jana, Z.-Y. Wu, K. Singh, A. Roy, P. Kumar, S. Maikap, J.-T. Qiu, H.-M. Cheng, L.-N. Tsai, Y.-L. Chang, R. Mahapatra and J.-R. Yang, *Sci. Rep.*, 2017, **7**, 4735.
59 S. A. E. Bashandy, M. A. Elbaset, F. A. A. Ibrahim, S. S. Abdelrahman, S. A. A. Moussa and A. M. A. El-Seidy, *Sci. Rep.*, 2025, **15**, 5709.
60 S. A. Bashandy, M. A. Elbaset, F. A. Ibrahim, S. A. A. Moussa, N. A. A. El-Latif, S. M. Afifi, T. Esatbeyoglu and A. M. El-Seidy, *J. Trace Elem. Miner.*, 2025, **14**, 100260.
61 A. Mohamed, A. A. Galhoum, A. Saad and S. Wageh, *Int. J. Biol. Macromol.*, 2025, **321**, 146329.
62 N. Hamad, A. A. Galhoum, A. Saad and S. Wageh, *J. Mol. Liq.*, 2024, **409**, 125349.
63 M. Sayyed, M. Mhareb, M. Hamad, A. J. Kadhim, K. M. Kaky and Y. Maghrbi, *Results Phys.*, 2025, **75**, 108356.
64 J. V. Gunha, A. Somer, S. d. R. F. Sabino, R. El-Mallawany, A. Novatski and R. F. Muniz, *Ceram. Int.*, 2025, **51**, 42377–42388.
65 G. Almisned, Z. Khattari, D. Sen Baykal, G. Susoy, G. Kilic, A. Ene and H. Tekin, *J. Mater. Res. Technol.*, 2023, **27**, 7582–7592.
66 M. M. Ismail, A. Darwish and H. Abo-Mosallam, *Ceram. Int.*, 2025, **51**, 42496–42508.
67 I. Mahmoud, M. Gaafar, S. Marzouk, A. Okasha and H. Elsaghier, *Phys. B*, 2025, **714**, 417526.
68 I. M. Nabil, A. M. A. El-Seidy, A. T. Mosleh, H. Y. Zahran, S. H. Zyoud and I. S. Yahia, *J. Mater. Sci.: Mater. Electron.*, 2024, **35**, year.

69 S. A. E. Bashandy, A. M. A. El-Seidy, F. A. A. Ibrahim, S. S. Abdelrahman, S. A. Abdelmottaleb Moussa and M. A. ElBaset, *Sci. Rep.*, 2023, **13**, 16010.
70 G. A. Alharshan, A. M. A. El-Seidy, M. I. Elamy, I. M. Nabil, A. M. El-Refaey, R. A. Elsad, M. S. Shams, A. M. Abdelghany and Y. S. Rammah, *J. Mater. Sci.: Mater. Electron.*, 2024, **35**, 862.
71 M. Abd Elwanees, *Mat. J. Vet. Med.*, 2023, **3**, 50–57.
72 M. A. E. M. Sayed, N. A. A. E. Latif, F. A. H. A. S. Ibrahim, A. M. A. El-Seidy, S. A. A. Moussa and S. A. E. M. Bashandy, *Braz. Arch. Biol. Technol.*, 2024, **67**, 1.